On-chip Circular Polarization Splitter Using Silicon Photonic Nanoantenna Array

Zhongjin Lin, Yuxuan Chen, Leslie Rusch, and Wei Shi

ACS Photonics, (Volume 5, Number 11) (2018)

Doi: 10.1021/acsphotonics.8b00522

https://pubs.acs.org/doi/abs/10.1021/acsphotonics.8b00522

On-chip Circular Polarization Splitter Using Silicon Photonic Nanoantenna Array

*Zhongjin Lin, Yuxuan Chen, Leslie Rusch, and Wei Shi**

Department of Electrical and Computer Engineering, Center of Optics, Photonics and Laser (COPL), Université Laval, Québec, Québec, G1V 0A6, Canada

ABSTRACT: Control and sorting of quantum states of photons through the manipulation of polarization and spatial modes of light in integrated photonic circuits contributes important applications in optical communications and quantum-optical systems. We design and demonstrate a novel structure for a silicon nanoantenna array that can split the circular polarization states, and couple them to separate single-mode silicon waveguides. Implemented using a CMOS-compatible photonic fabrication process, the array can be monolithically integrated with other photonic components for chip-scale optical signal processing. We also show that the polarization sorting property of the nanoantenna array can be flexibly controlled (by adjusting design parameters at subwavelength scale) to split any two arbitrary orthogonal polarization states.

KEYWORDS: integrated photonic circuits, nano-optics, optical communication, chip-scale, spin-orbit interactions

Polarization, corresponding to spin angular momentum, is one of the most important intrinsic properties of light.[1-2] Specifically, right-handed and left-handed circular polarizations represent the two spin states of photons. Manipulating and measuring the spin of photons has application in many fields, such as remote sensing,[3] optical communications,[4] and quantum computing systems[5]. While polarizers and waveplates are traditionally used to produce and analyze polarized light, recently, nano-optic structures, such as plasmonic structures and dielectric metasurfaces, have been proposed to monitor and manipulate polarization states through spin-orbit interactions at sub-wavelength scale. [1, 6-7] However, these devices usually stand alone without coupling into integrated photonic circuits. During the last decade, silicon photonics has quickly emerged to enable large-

scale photonic integration using CMOS-compatible semiconductor processes.[8-9] Linear polarization diversity has been examined for optical interconnects.[10-12] It has also been shown that circularly polarized light can be generated by combining a linear-polarization grating coupler and an interferometer circuit.[13] However, there has been little investigation on direct detection of circular polarizations in silicon photonics.

In this letter, we present an integrated circular-polarization splitter using a silicon nanoantenna array on the standard 220 nm silicon-on-insulator (SOI) platform. A fishbone pattern is adopted in our design. Metallic fishbone nanoantennas have been used for polarization-controlled directional coupling[14-18] and beam steering[19]. Here, we demonstrate, for the first time, a 2D silicon fishbone nanoantenna array (Si-FBNA) that not only resolves the circular polarization state, but also couples those orthogonal polarization states directly into separate single-mode waveguides integrated on the same chip. Integration into the silicon photonic integrated circuits (PICs) is a great advantage, allowing the Si-FBNA to work together with many other silicon photonic components, such as high-speed modulators,[20] optical filters,[21] interferometers,[22-23] etc., to produce more advanced chip-scale information processing in the optical domain.

The schematic of the proposed 2D Si-FBNA system is shown in Fig. 1(a). Two single-mode waveguides are located to either side of the Si-FBNA. The desired directional coupling is in the longitudinal direction, defined as the *x*-axis; the lateral direction of the waveguides on the chip plane is defined as the *y*-axis. As shown in Fig. 1(b), the Si-FBNA consists of a number of sub-wavelength silicon scattering elements buried in SiO_2, each being 200 nm in width (w) and 450 nm in length (L). Each column is arranged in a fishbone pattern with 408 nm spacing (S) between adjacent elements orientated in orthogonal directions. The spacing is chosen so that $2S$ is equal to $3\lambda_0/(2n_{eff,\,y})$, where λ_0 is the wavelength of incident light in the vacuum and $n_{eff,\,y}$ is the effective index in the *y*-direction; this choice suppresses optical coupling in the undesired direction (*y* in this case). The period of columns, Λ, is an optimization parameter for the control of the polarization sorting property and will be discussed in detail later. Linear tapers are used to couple the light from the nanoantenna array to the single-mode waveguides (220 nm in height and 500 nm in width) with a gap (g) of 200 nm in-between.

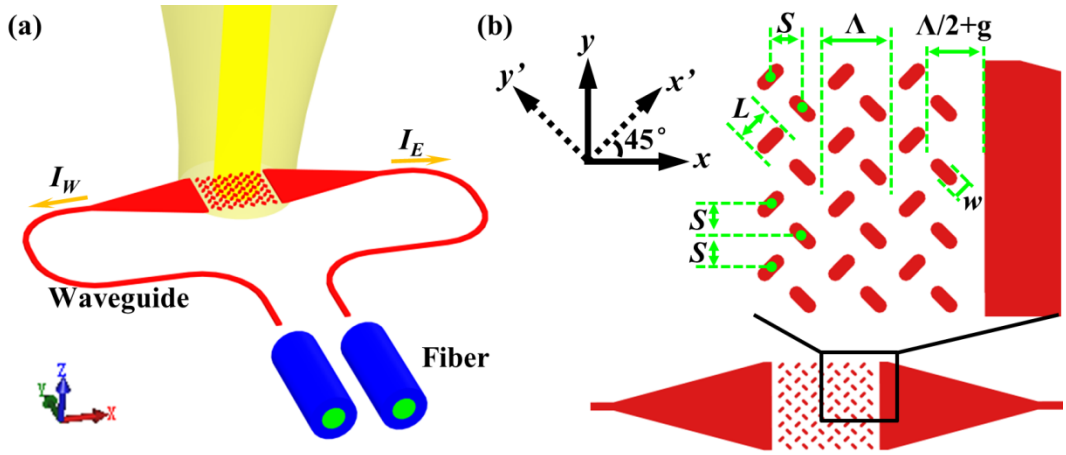

Figure 1. (a) Schematic of the proposed silicon fishbone nanoantenna array system with light coupling vertically and sorted polarizations exiting to waveguides to west and east; (b) vertical view of the array and the key physical parameters.

The principle of the proposed Si-FBNA is given as follows using a simple formalism based on the Jones vector. Assuming polarized light with an electric field $\vec{E}$ is incident normal to the surface of the chip, the components of the incident field projected on *x*'-axis and *y*'-axis having an angle of 45° and 135° with respect to the *x*-axis, respectively (see the coordinate frames in Fig. 1(b)), can be described as

$$\begin{pmatrix} E_{x'} \\ E_{y'} \end{pmatrix} = A \begin{pmatrix} \cos\alpha \\ \sin\alpha \cdot e^{i\delta} \end{pmatrix} \tag{1}$$

The amplitude of the incident *E*-field is given by a constant *A*. We can describe all the polarization states via (1) in a polar coordinate system with α ($0 \le \alpha < 2\pi$) and δ ($0 \le \delta < \pi$) as the angular and radial coordinates, respectively; i.e., (α, δ) corresponds to a specific polarization state. For example, ($\pi/4$, $\pi/2$) represents left-handed circular polarization (LHCP), while ($3\pi/4$, $\pi/2$) indicates right-handed circular polarization (RHCP). Two polarizations (α_1, δ_1) and (α_2, δ_2) are orthogonal if they satisfy

$$\begin{pmatrix} \cos\alpha_1 \\ \sin\alpha_1 \cdot e^{i\delta_1} \end{pmatrix}^T \begin{pmatrix} \cos\alpha_2 \\ \sin\alpha_2 \cdot e^{i\delta_2} \end{pmatrix}^* = 0 \tag{2}$$

where *T* denotes transpose and an asterisk denotes complex conjugate. Orthogonality requires$\delta_1 = \delta_2$ and $\alpha_1 - \alpha_2 = (m+1/2)\,\pi$ where *m* is an integer.

The optical wave propagating to the west (E_W) waveguide and the east (E_E) waveguide in Fig. 1 can be obtained by[14]

$$\begin{pmatrix} E_W \\ E_E \end{pmatrix} \propto A \begin{pmatrix} C_1 & C_2 e^{iS\square\beta} \\ C_2 e^{iS\square\beta} & C_1 \end{pmatrix} \begin{pmatrix} \cos\alpha \\ \sin\alpha \cdot e^{i\delta} \end{pmatrix} \tag{3}$$

where C_1 and C_2 are the coupling coefficients of the nanoantenna array, β is the *x*-directional propagation constant within the nanoantenna array related to the *x*-directional effective index $n_{eff,\,x}$ by,

$$\beta = \frac{2\pi n_{eff,x}}{\lambda_0} \tag{4}$$

where λ_0 is the wavelength of incident light in the vacuum. Although the nanoantenna array has translational symmetry, it does not have mirror symmetry. Thus, C_1 is not necessarily equal to C_2 (a detailed discussion is given in Support Information II). Here, we set $C = C_1 = \kappa C_2$, where the κ parameterizes the asymmetry of the directional coupling. Then the field intensities I_E and I_W can be written as

$$I_W \propto \left|A \cdot C\right|^2 \left[\left(\cos^2\alpha + \kappa^2 \sin^2\alpha\right) + \kappa \cdot \sin 2\alpha \cdot \cos(\delta + S \cdot \beta)\right] \tag{5}$$

$$I_E \propto \left|A \cdot C\right|^2 \left[\left(\kappa^2 \cos^2\alpha + \sin^2\alpha\right) + \kappa \cdot \sin 2\alpha \cdot \cos(\delta - S \cdot \beta)\right] \tag{6}$$

From this, power difference between I_W and I_E is proportional to

$$\left(I_W - I_E\right) \propto \left|A \cdot C\right|^2 \left[\left(1-\kappa^2\right)\cos 2\alpha - 2\kappa \cdot \sin 2\alpha \cdot \sin\delta \cdot \sin\left(S \cdot \beta\right)\right] \tag{7}$$

which can be rewritten as

$$\left(I_W - I_E\right) \propto \left|A \cdot C\right|^2 \cdot B \cdot \sin\left[2\left(\alpha + \varphi\right)\right] \tag{8}$$

where,

$$B = \sqrt{\left(1-\kappa^2\right)^2 + \left[2\kappa \cdot \sin\delta \cdot \sin\left(S \cdot \beta\right)\right]^2} \tag{9}$$

$$\cos 2\varphi = \frac{-2\kappa \cdot \sin\delta \cdot \sin\left(S \cdot \beta\right)}{\sqrt{\left(1-\kappa^2\right)^2 + \left[2\kappa \cdot \sin\delta \cdot \sin\left(S \cdot \beta\right)\right]^2}} \tag{10}$$

Notably, (I_W - I_E) shows a sinusoidal variation, with period π, as a function of the angle α. Its axis of symmetry is at $\alpha = n\pi/4 - \varphi$ (where n is an integer). Per Eq. (7), κ and β are the keys to determining the polarization sorting properties of the nanoantenna array.

Full-wave finite difference time domain (FDTD) simulations are performed to study the influence of the fishbone column period, Λ, on the parameters κ and β. For these simulations, the relative phase δ is 90°, center wavelength λ_0 is 1550 nm, and input power is 1 mW. The simulated (I_W - I_E) at different Λ and α is shown in Fig. 2(a). For fixed δ, as α is swept, the total polarization changes. Above the graph in Fig. 2(a), we see a sketch of polarization states for α values at the vertical dashed lines; double ended lines represent linear polarizations. The circles represent circular polarization. The arrows indicate the direction of polarization. The color bar is used to indicate whether the output power is directed entirely to the east output port (deep blue), or the west output port (deep red), or some mix. We can observe that the polarization sorting properties of the nanoantenna array vary with Λ. In all cases, (I_W - I_E) shows a sinusoidal variation as a function of the angle α with a period of π, as predicted by Eq. (8). The conversion efficiency, defined as the ratio of the total power coupled into the two waveguides to the input power, is about 1%; near 98% of the input optical power penetrates through the structure. Many applications require a higher conversion efficiency that can be achieved by matching the antenna-array mode profile with the input beam and by engineering the wafer (e.g., adding a backside metal mirror[24]). The array distribution and its footprint may also be optimized through an inverse design[12, 25].

When α = 0 (linearly polarized in *x'*), κ can be calculated by Eq. (5) and (6) as a function of Λ; see Fig. 2(b). From that figure, we observe that for this simulation, κ varies between 0.7 and 2.3 as Λ varies from 1 μm to 2 μm. Using κ found in Fig. 2(b) and (I_W - I_E) shown in Fig. 2(a), the term sin($S\cdot\beta$) in Eq. (5) and (6) can be calculated by

$$\sin\left(S\cdot\beta\right)=\frac{\kappa\cdot\left(I_W-I_E\right)_{\delta=90^\circ,\alpha=45^\circ}}{-2\left(I_E\right)_{\delta=90^\circ,\alpha=0^\circ}} \tag{11}$$

The curve in Fig. 2(c) describes the relationship between sin($S\cdot\beta$) and Λ.

According to the values of κ and sin($S\cdot\beta$), which are determined by the design parameters and the operating wavelength, the polarization sorting properties of the nanoantenna array can be grouped into three situations. The first one is κ = 1, which occurs for Λ = 1.54 μm. The second one is $\kappa \neq 1$ and sin($S\cdot\beta$) = 0, which occurs for Λ = 2 μm. The last one is a more general situation when $\kappa \neq 1$ and sin($S\cdot\beta$) $\neq 0$ and several values of Λ could hold. To observe nanoantenna behavior in

these situations, we run a new series of simulations, allowing α and δ to vary, and examining three values of Λ: 1.54 μm, 2 μm, and 1 μm.

Consider LHCP with $\alpha = \pi/4$, $\delta = \pi/2$. For the first case with $\kappa = 1$, in Fig. 3(a) this point is deep blue, indicating all light is directed to the east output port. Similarly, RHCP light is deep red, indicating all light is directed to the west output port. The Si-FBNA can identify whether the incident light is left-handed (LH) or right-handed (RH).

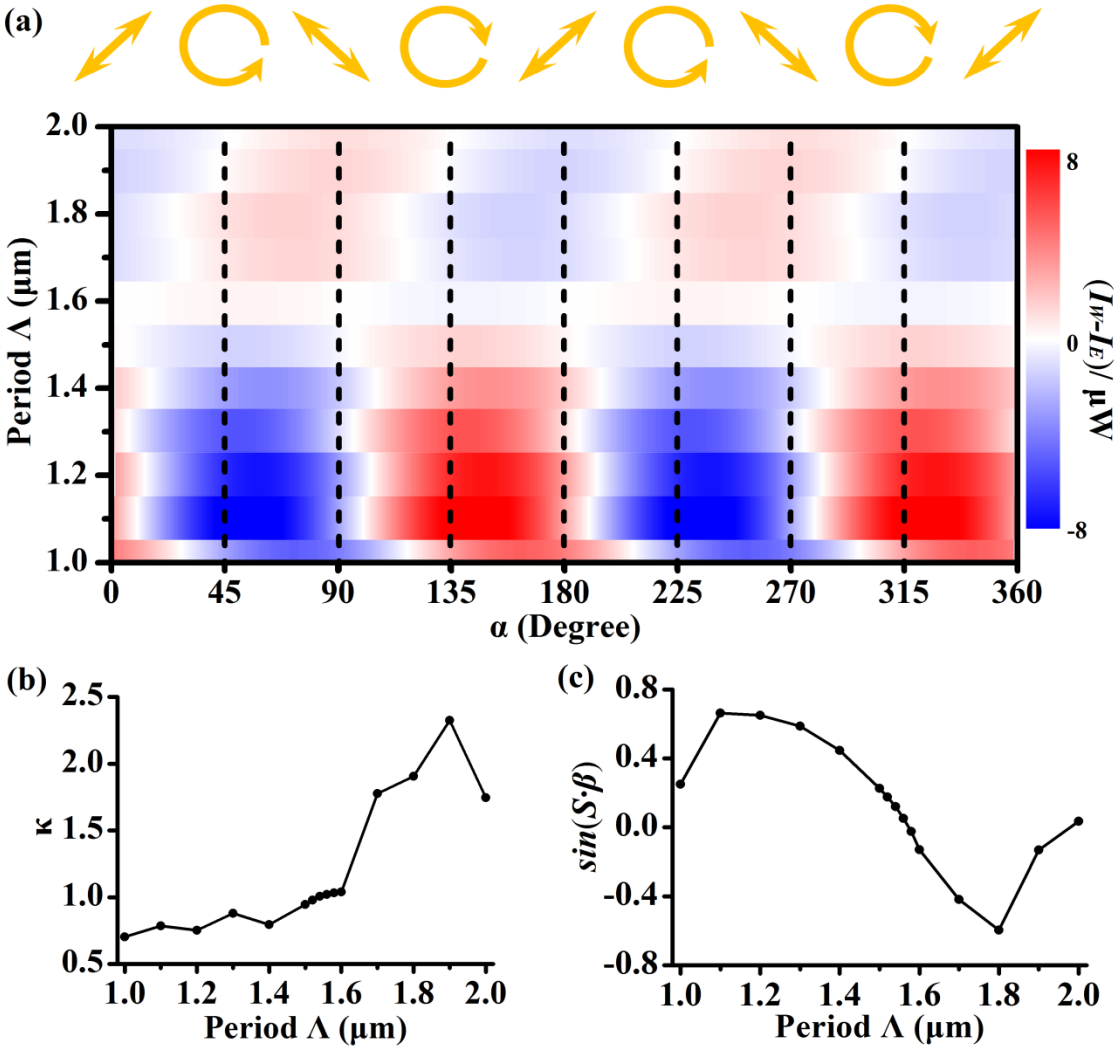

Figure 2. For relative phase $\delta = 90°$ and input power 1 mW: (a) (I_W - I_E) at swept periods Λ and projection angles α; (b) κ vs. Λ; and (c) sin($S \cdot \beta$) vs. Λ.

For the second situation with $\kappa \neq 1$ and sin($S \cdot \beta$) = 0, (I_W - I_E) is determined by $(1 - \kappa^2) \cdot \cos 2\alpha$ and is invariant in the relative phase δ between $E_{x'}$ and $E_{y'}$. Therefore, this specific design can be used to estimate the α parameter of the polarized light. The simulated results are shown in Fig. 3(b).

When α falls in the range from $\pi/4 + n\pi$ to $3\pi/4 + n\pi$ (where n is an integer), $(I_W - I_E)$ is positive. For other angles, $(I_W - I_E)$ is negative.

For the last situation with $\kappa \neq 1$ and $\sin(S \cdot \beta) \neq 0$, the period $\Lambda = 1$ μm is taken as an example. In this case, $\kappa = 0.702$ and $\sin(S \cdot \beta) = 0.435$. Figure 3(c) shows the simulated results. As shown in Eq. (7), $(I_W - I_E)$ is determined by two terms: $(1 - \kappa^2) \cdot \cos 2\alpha$, and $2\kappa \cdot \sin 2\alpha \cdot \sin\delta \cdot \sin\theta$. Compared to the first case ($\kappa = 1$), the axis of symmetry is rotated to near $\alpha = 70°$ instead of 45°. This means that the choice of κ and $\sin(S \cdot \beta)$ allows us to target separation of any two orthogonal polarizations.

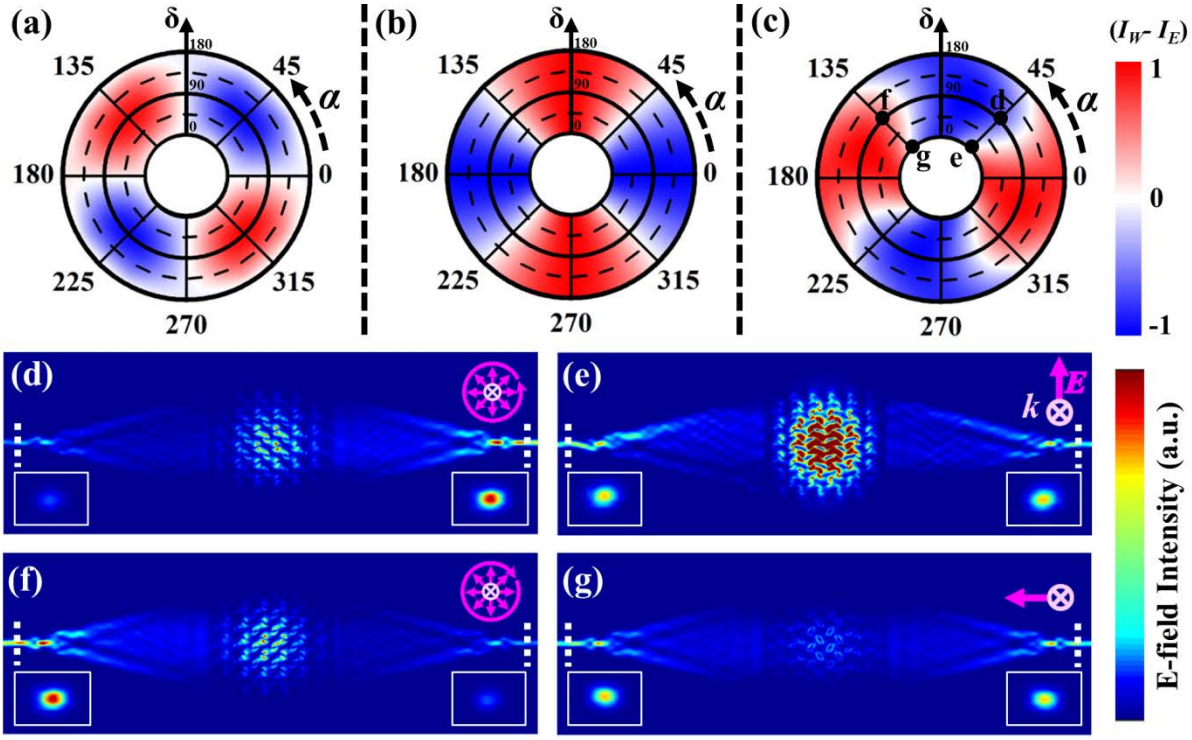

Figure 3. $(I_W - I_E)$ as a function of the polarization state (α, δ) for (a) $\Lambda = 1.54$ μm, (b) $\Lambda = 2$ μm and (c) $\Lambda = 1$ μm; and, for $\Lambda = 1$ μm, the field intensity distributions when inputting: (d) LHCP, (e) linear vertical, (f) RHCP and (g) linear horizontal polarization; lower insets in (d)-(g) on the far left and far right show transverse electric-field intensity distributions of the coupled optical waves propagating in the west (far left) and east (far right) waveguides, and upper right insets sketch the polarization state.

Continuing with the case of $\Lambda = 1$ μm, Fig. 3(d)-(g) give the electric field intensity distribution over the plane of the nanoantenna for various incident polarizations. The west output port is found to the far left, and the east output port to the far right; transverse intensities at these ports are shown as lower insets. A sketch of the incident polarization is given in the upper inset of each subplot:

LHCP, linear vertical, RHCP and linear horizontal polarization, for Fig. 3(d)-(g), respectively. We can clearly observe that the optical waves propagating in the west and east waveguides are different under the various incident polarizations. They show good agreement with the predictions of Eq. (7). For example, for LHCP, shown in Fig. 3(d), the intensity of the optical field coupled into the west waveguide is clearly much weaker than that coupled into the east waveguide, as seen in transverse fields and in the planar display. LHCP is well coupled to the fundamental TE mode of the east waveguide with little crosstalk in the other waveguide. This unidirectional coupling of circular polarization establishes the capacity of the Si-FBNA to split the circularly polarized light.

The devices with $\Lambda = 1.54$ μm and $\Lambda = 1$ μm were fabricated using electron-beam lithography. As discussed above, the design $\Lambda = 1.54$ μm sorts right and left circular polarizations, while $\Lambda = 1$ μm was chosen to demonstrate the Eq. (7). We employ fiber grating couplers[26] to couple light into and out of the silicon photonic chip. All the components, including the Si-FBNA, waveguides and grating couplers, were made of a 220 nm-thick SOI wafer with a 2 μm buried oxide and a 2 μm oxide cladding. Figure 4 shows the scanning electron microscope (SEM) image of the fabricated Si-FBNA devices. Figure 4(a) shows the structure of the Si-FBNA device, including the output waveguides. Figures 4(b) and (c) show the details of the Si-FBNAs, with $\Lambda = 1$ μm and $\Lambda = 1.54$ μm, respectively. The devices were characterized using light from a laser ($\lambda_0 = 1550$ nm) irradiating the antenna array at normal incidence. The polarization of the light incident to the antenna array was adjusted with a series of polarizers, quarter-wave plates and half-wave plates (details are given in Supplementary IV). The outputs from the waveguides were coupled out of the chip using 1D grating couplers, which were then collected and detected using an optical fiber array coupled to a photo-detector (EXFO Optical Test System IQ 203). The conversion efficiency depends on the input polarziation state and was measured to be 1.1% at its maximum, showing a good agreement with the simulation. Details for the measurement of conversion efficiency with the calibration of the output grating couplers and the input beam profile are presented in section V of Supplementary.

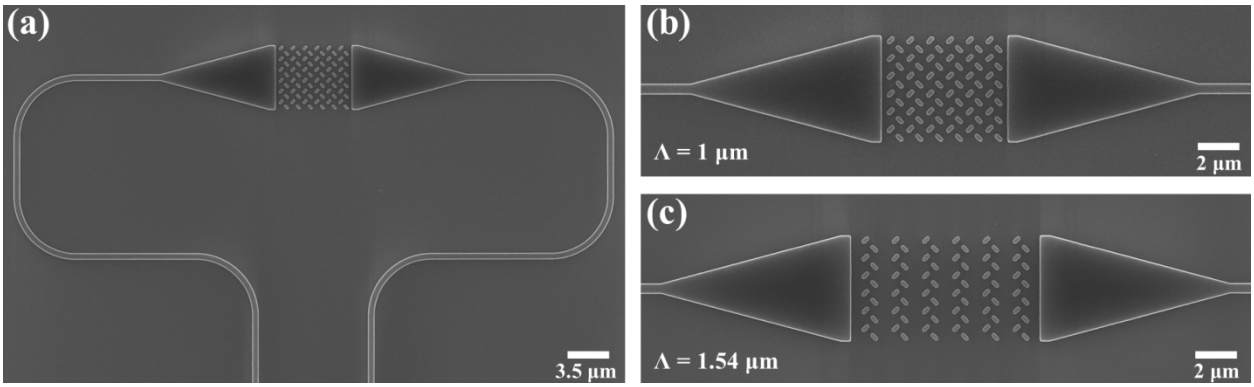

Figure 4. The SEM images: (a) silicon fishbone nanoantenna array with the output waveguides; (b), (c) zoom-in for Λ = 1 μm and Λ = 1.54 μm, respectively.

Figures 5(a) and (b) show the measured (I_W - I_E) under linear polarization ($\delta = 0^o$) and elliptic polarization inputs ($\delta = 90^o$), respectively. Their corresponding simulated results are also shown. The results of (I_W - I_E) have been normalized to their respective maximum achieved at $\delta = 90^o$ (Eq. 12 shown in following) to best illustrate their different responses to various polarization states.

$$\frac{\left(I_W - I_E\right)}{\max\left(I_W - I_E\right)} \propto \frac{\left[\left(1-\kappa^2\right)\cos 2\alpha - 2\kappa \cdot \sin 2\alpha \cdot \sin\delta \cdot \sin\left(S \cdot \beta\right)\right]}{\sqrt{\left(1-\kappa^2\right)^2 + \left[2\kappa \cdot \sin\left(S \cdot \beta\right)\right]^2}}. \tag{12}$$

As expected, (I_W - I_E) always undergoes a sinusoidal variation with the projection angle α for the same relative phase δ. We can observe that the measured results agree well with simulations. In the case of Λ = 1 μm (blue solid line shown in Fig. 5), the main difference in (I_W - I_E) between the $\delta = 0^o$ and $\delta = 90^o$ is the initial phase of the sinusoidal function. In the case of Λ = 1.54 μm and $\delta = 90°$ (red solid line shown in Fig. 5(b)), the maximum and minimum (I_W - I_E) are at the RHCP and LHCP, respectively. This confirms its capacity to split the circular polarization states. Note that since the conversion efficiency is in general polarization dependent, unlike the direct differential output, (I_W - I_E)/(I_W + I_E) does not always show a sinusoidal behavior (as shown in Fig. S7 of Supplementary).

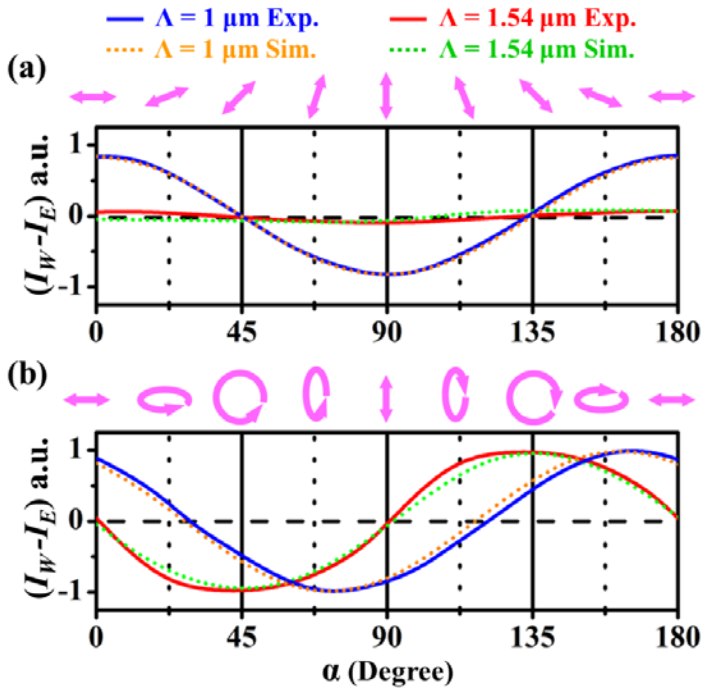

Figure 5. Measured and simulated results of normalized (I_W - I_E) as a function of the projection angle α for Λ = 1 μm and Λ = 1.54 μm when (a) δ = 0° and (b) δ = 90°. (Blue solid line and orange dashed line are the experiment and simulation results, respectively for the structure of Λ = 1 μm; red solid line and green dashed line are the experiment and simulation results, respectively for the structure of Λ = 1.54 μm.) The pink sketches above the graphs represent the polarization state for the α for the vertical lines.

In summary, a novel structure of nanoantenna array, namely a Si-FBNA, has been proposed and experimentally demonstrated on a standard silicon photonics platform. We have shown that this structure can split the circular polarization states and couple them directly to separate single-mode silicon waveguides. The polarization sorting property of such a nanoantenna array can be designed to split any arbitrary pair of orthogonal polarization states. The integration of the proposed device in silicon PICs is a great advantage over previously proposed devices, as it can be combined with other photonic components on the same platform for chip-scale optical signal processing. This makes it attractive for a number of applications requiring manipulation of polarization states of photons, such as quantum key distribution[27], in-line polarimeter[28], and polarization shift keying for high-capacity optical communications[29]. In particular, the capacity to split circular polarizations can be used for on-chip detection or (de-)multiplexing of orbital angular momentum modes carried by circularly polarized light in optical fibers.[30]

ASSOCIATED CONTENT

Supporting Information

The supplementary include: “The Layout of Device”, “The Influence of Position’s Asymmetry on the Coupling Coefficient”, “Jones Calculus and the detail of experiment”, “The measured conversion efficiency”, and “$(I_W - I_E)/(I_W + I_E)$ vs α”. These materials are available free of charge via the Internet at http://pubs.acs.org.

AUTHOR INFORMATION

Corresponding Author

* E-mail: wei.shi@gel.ulaval.ca

Author Contributions

The manuscript was written through contributions of all authors. All authors have given approval to the final version of the manuscript.

Funding Sources

This project is supported by the Natural Science and Engineering Research Council (NSERC) of Canada.

Notes

The authors declare no competing financial interest.

ACKNOWLEDGMENT

Zhongjin Lin would like to thank the support from the China Scholarship Council (NO. 201606890030). We thank Alessandro Corsi for his help in the manuscript revision.

REFERENCES

(1) Bliokh, K. Y.; Rodríguez-Fortuño, F. J.; Nori, F.; Zayats, A. V., Spin–orbit interactions of light. *Nature Photonics* **2015,** *9* (12), 796-808.
(2) Willner, A. E.; Huang, H.; Yan, Y.; Ren, Y.; Ahmed, N.; Xie, G.; Bao, C.; Li, L.; Cao, Y.; Zhao, Z.; Wang, J.; Lavery, M. P. J.; Tur, M.; Ramachandran, S.; Molisch, A. F.; Ashrafi, N.; Ashrafi, S., Optical communications using orbital angular momentum beams. *Advances in Optics and Photonics* **2015,** *7* (1), 66.
(3) Tyo, J. S.; Goldstein, D. L.; Chenault, D. B.; Shaw, J. A., Review of passive imaging polarimetry for remote sensing applications. *APPLIED OPTICS* **2000,** *45* (22).
(4) Song, S.; Wang, C., Recent development in quantum communication. *Chinese Science Bulletin* **2012,** *57* (36), 4694-4700.
(5) Slussarenko, S.; Weston, M. M.; Li, J. G.; Campbell, N.; Wiseman, H. M.; Pryde, G. J., Quantum State Discrimination Using the Minimum Average Number of Copies. *Physical review letters* **2017,** *118* (3), 030502.
(6) Genevet, P.; Capasso, F.; Aieta, F.; Khorasaninejad, M.; Devlin, R., Recent advances in planar optics: from plasmonic to dielectric metasurfaces. *Optica* **2017,** *4* (1), 139.
(7) Pu, M.; Li, X.; Ma, X.; Wang, Y.; Zhao, Z.; Wang, C.; Hu, C.; Gao, P.; Huang, C.; Ren, H.; Li, X.; Qin, F.; Yang, J.; Gu, M.; Hong, M.; Luo, X., Catenary optics for achromatic generation of perfect optical angular momentum. *Advanced Science* **2015,** *1*, 1500396.
(8) Simply silicon. *Nature Photonics* **2010,** *4* (8), 491-491.
(9) Sun, J.; Timurdogan, E.; Yaacobi, A.; Hosseini, E. S.; Watts, M. R., Large-scale nanophotonic phased array. *Nature* **2013,** *493* (7431), 195-9.
(10) Wang, J.; Bonneau, D.; Villa, M.; Silverstone, J. W.; Santagati, R.; Miki, S.; Yamashita, T.; Fujiwara, M.; Sasaki, M.; Terai, H.; Tanner, M. G.; Natarajan, C. M.; Hadfield, R. H.; O'Brien, J. L.; Thompson, M. G., Chip-to-chip quantum photonic interconnect by path-polarization interconversion. *Optica* **2016,** *3* (4), 407.
(11) Piekarek, M.; Bonneau, D.; Miki, S.; Yamashita, T.; Fujiwara, M.; Sasaki, M.; Terai, H.; Tanner, M. G.; Natarajan, C. M.; Hadfield, R. H.; O'Brien, J. L.; Thompson, M. G., High-extinction ratio integrated photonic filters for silicon quantum photonics. *Optics letters* **2017,** *42* (4), 815-818.
(12) Piggott, A. Y.; Lu, J.; Babinec, T. M.; Lagoudakis, K. G.; Petykiewicz, J.; Vuckovic, J., Inverse design and implementation of a wavelength demultiplexing grating coupler. *Scientific reports* **2014,** *4*, 7210.
(13) He, L.; Li, M., On-chip synthesis of circularly polarized emission of light with integrated photonic circuits. *Optics letters* **2014,** *39* (9), 2553-6.
(14) Lin, J.; Mueller, J. P.; Wang, Q.; Yuan, G.; Antoniou, N.; Yuan, X. C.; Capasso, F., Polarization-controlled tunable directional coupling of surface plasmon polaritons. *Science* **2013,** *340* (6130), 331-4.
(15) Chang, C. W.; Lin, C. E.; Yu, C. J.; Yeh, T. T.; Yen, T. J., Miniature Surface Plasmon Polariton Amplitude Modulator by Beat Frequency and Polarization Control. *Scientific reports* **2016,** *6*, 32098.
(16) Chen, B.; Yang, J.; Hu, C.; Wang, S.; Wen, Q.; Zhang, J., Plasmonic polarization nano-splitter based on asymmetric optical slot antenna pairs. *Optics letters* **2016,** *41* (21), 4931.
(17) Du, L.; Kou, S. S.; Balaur, E.; Cadusch, J. J.; Roberts, A.; Abbey, B.; Yuan, X. C.; Tang, D.; Lin, J., Broadband chirality-coded meta-aperture for photon-spin resolving. *Nat Commun* **2015,** *6*, 10051.

(18) Mueller, J. P.; Leosson, K.; Capasso, F., Polarization-selective coupling to long-range surface plasmon polariton waveguides. *Nano letters* **2014,** *14* (10), 5524-7.
(19) Lindfors, K.; Dregely, D.; Lippitz, M.; Engheta, N.; Totzeck, M.; Giessen, H., Imaging and Steering Unidirectional Emission from Nanoantenna Array Metasurfaces. *ACS Photonics* **2016,** *3* (2), 286-292.
(20) Dubé-Demers, R.; LaRochelle, S.; Shi, W., Ultrafast pulse-amplitude modulation with a femtojoule silicon photonic modulator. *Optica* **2016,** *3* (6), 622.
(21) Shi, W.; Yun, H.; Lin, C.; Greenberg, M.; Wang, X.; Wang, Y.; Fard, S. T.; Flueckiger, J.; Jaeger, N. A. F.; Chrostowski, L., Ultra-compact, flat-top demultiplexer using anti-reflection contra-directional couplers for CWDM networks on silicon. *Optics express* **2013,** *21* (6), 6733-6738.
(22) Green, W. M. J.; Rooks, M. J.; Sekaric, L.; Vlasov, Y. A., Ultra-compact, low RF power, 10 Gb/s silicon Mach-Zehnder modulator. *Optics express* **2007,** *15* (25), 17106-11713.
(23) Wilkes, C. M.; Qiang, X.; Wang, J.; Santagati, R.; Paesani, S.; Zhou, X.; Miller, D. A.; Marshall, G. D.; Thompson, M. G.; O'Brien, J. L., 60 dB high-extinction auto-configured Mach-Zehnder interferometer. *Optics letters* **2016,** *41* (22), 5318-5321.
(24) Zaoui, W. S.; Rosa, M. F.; Vogel, W.; Berroth, M.; Butschke, J.; Letzkus, F., Cost-effective CMOS-compatible grating couplers with backside metal mirror and 69% coupling efficiency. *Optics express* **2012,** *20* (26), B238- B243.
(25) Su, L.; Piggott, A. Y.; Sapra, N. V.; Petykiewicz, J.; Vučković, J., Inverse Design and Demonstration of a Compact on-Chip Narrowband Three-Channel Wavelength Demultiplexer. *ACS Photonics* **2017,** *5* (2), 301-305.
(26) Wang, Y.; Yun, H.; Lu, Z.; Bojko, R.; Shi, W.; Wang, X.; Flueckiger, J.; Zhang, F.; Caverley, M.; Jaeger, N. A. F.; Chrostowski, L., Apodized Focusing Fully Etched Subwavelength Grating Couplers. *IEEE Photonics Journal* **2015,** *7* (3), 1-10.
(27) Sibson, P.; Kennard, J. E.; Stanisic, S.; Erven, C.; O'Brien, J. L.; Thompson, M. G., Integrated silicon photonics for high-speed quantum key distribution. *Optica* **2017,** *4* (2), 172.
(28) Balthasar Mueller, J. P.; Leosson, K.; Capasso, F., Ultracompact metasurface in-line polarimeter. *Optica* **2016,** *3* (1), 42.
(29) Zhao, X.; Yao, Y.; Sun, Y.; Liu, C., Circle Polarization Shift Keying With Direct Detection for Free-Space Optical Communication. *J. OPT. COMMUN. NETW* **2009,** *1* (4), 307-312.
(30) Chen, Y.; Rusch, L. A.; Shi, W., Integrated Circularly Polarized OAM Generator and Multiplexer for Fiber Transmission. *IEEE Journal of Quantum Electronics* **2017**, 1-1.